CHAPTER 1

INTRODUCTION

1.1 Background

Noble metals supported on oxides are used in many applications such as paintings, cosmetics, pharmaceuticals, ceramics, electronics, photocatalysts, and sensors. Flame spray pyrolysis (FSP) is known as a method for one-step synthesis and deposition of catalysts onto surfaces of the support nanoparticles [1]. FSP is described in more details by Mädler *et al*. [2]. FSP was successfully employed for the preparation of pure TiO_2, Zn/TiO_2 [3], Fe/TiO_2 [4], Au/TiO_2 [5, 6], Nb and Cu/TiO_2 [7], Pt/TiO_2 [8], WO_3/TiO_2 [9]. The mechanisms of a spray flame synthesis are explained as it was employed to produce the nanostructured particles.

Titanium dioxide is one of the most promising candidates for gas sensor [10–12] due to its cheapness, stability and environmental safety. Titanium dioxide (TiO_2) is an n-type semiconductor material [13] (Eg = 3.2 eV (anatase) and Eg = 3.0 eV (rutile)) with the absorption edge below 400 nm [14]. The sensing properties are based on reactions between semiconductor oxides and gases in the atmosphere. These reactions produce changes in electrical properties of semiconductors and hence analyte detection is signaled by a change in the electrical conductivity of the sensor film [15–18].

Sensitivity of TiO_2 sensors can be improved by addition of dopants such as Ta, Pt, V_2O_5, Li, La, Co, Cu, Nb, Cu, Cr, Ag, Au [19–28], The most important effect of dopant addition in TiO_2 is increasing the conductivity, slowing down anatase to rutile

transformation and reducing grain growth. We emphasize on the noble metal nanoparticles because noble metal nanoparticles have earned their reputation as the excellent catalyst in gas sensing performances [28–30].

Here, metal supported catalysts are of main interest. This is because the addition of a noble metal helps enhance sensitivity/selectivity of sensors. The role of the metal in enhancing the sensitivity and response rate of the sensor element could be due to the electronic interaction between the sensitizer and the semi-conducting material. Little attention had been paid to TiO_2 as a gas sensor material for inflammable gas detection until the end of 1990s due to its rather inert surface properties and high intrinsic resistivity, in comparison with conventional sensor materials, such as SnO_2 and ZnO. However, recent progress in nanotechnology raises active research on this material. Various types of nanostructured TiO_2, such as nanoporous films [31–36] and nanotubes [37, 38] have been prepared and tested as gas sensors for H_2 or other flammable gases. An increase in the surface to volume ratio induced by the nano-control may be responsible for the improvement of sensing properties of these sensors. In connection with such a trend in gas sensors, TiO_2 thin films with submicron-size pores were prepared by anodic oxidation of a Ti plate and then evaluated their gas-sensing properties of the configuration of M (M = Pd, Pt and Au)/TiO_2/Ti electrode [39–41].

In present study, a promoting way to prepare selective and sensitive gas sensor based on metal (Pt, Au and Ag)-loaded TiO_2 is presented, and the gas responses towards different oxidizing and reducing gases are comparatively investigated.

1.2 Titanium dioxide (TiO_2)

Titanium dioxide or titania is the naturally occurring oxide of titanium. It is an inorganic compound with the formula TiO_2. The 3 crystalline structures of TiO_2 are anatase (tetragonal), rutile (tetragonal) and brookite (orthorhombic) and each of any phase have the unique physical and chemical properties [42–44]. A schematic presentation of the crystalline structure of TiO_2 was shown in Figure 1.1.

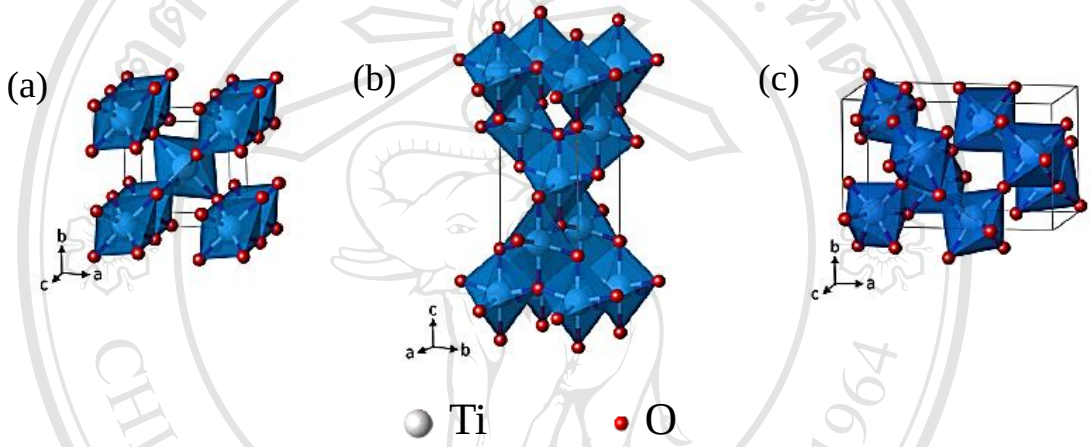

Figure 1.1 Schematic model of TiO_6 polyhedra for the TiO_2 phases rutile (a), anatase (b) and brookite (c) (Ti (white); O (red)) [44].

The three crystalline structures differ by the distortion of each octahedral and by the assembly patterns of the octahedral chains. The most common representation is the view of the crystal structures as networks of edge- and/or corner-linked distorted TiO_6 octahedron building blocks. Anatase has four edges sharing per octahedron but no corner oxygen sharing. The arrangement of these octahedral gives the overall structure of anatase. In the rutile phase, two edges are shared forming a linear chain. The linear chains are joined to each other by sharing of corner oxygen atom, producing the overall rutile structure. The octahedral linkages in brookite are such that three edges are shared

per octahedron. It has been envisioned that the joining together of these distorted TiO_6^{2-} octahedral forms the overall structure of brookite [43]. Table 1.1 outline the general properties of rutile, anatase phases of TiO_2.

Table 1.1 Types and physical properties of titanium dioxide [45].

Properties	**Titanium dioxide**	
	Rutile	**Anatase**
Crystal structure	Tetragonal	Tetragonal
Density (kg m^{-3})	4250	3894
Atoms per unit cell (Z)	2	4
Space group	$p\frac{4_2}{m}$nm	$l\frac{4}{a}$md
Atomic weight	79.890	79.890
Lattice parameters (nm)	a = 0.4594, c = 0.2958	a = 0.3785, c = 0.9514
Unit cell volume (nm3)a	0.0624	0.1363
Calculated indirect band gap (eV), (nm)	3.02–3.24, 382.7–410.1	3.23–3.59, 345.4–383.9
Experimental band gap (eV), (nm)	~3.0 ~413	~3.2 ~387
Refractive index	2.79, 2.903	2.54, 2.49

Table 1.1 (Cont.) Types and physical properties of titanium dioxide [45].

Properties	**Titanium dioxide**	
	Rutile	**Anatase**
Solubility in H_2O	Insoluble	Insoluble
Solubility in HF	Insoluble	Soluble
Melting point (°C)	1825	Transformation to rutile

1.3 Platinum (Pt) [46–49]

Platinum is a chemical element, malleable, silvery white, with the chemical symbol Pt and an atomic number of 78 as shown in the Figure 1.2. It is found mainly as the isotopes with atomic weights of 194, 195 and 196, with a maximum oxidation state of +6, the oxidation states of +2 and +4 being the most stable. While the metal does not corrode in air at any temperature, it can be affected by halogens, cyanides, sulfur, molten sulfur compounds, heavy metals and hydroxides [46]. Platinum, a precious transition metal that has outstanding catalytic and electrical properties and superior resistant characteristics to corrosion, has been widely applied in chemical, petrochemical, pharmaceutical, electronic, and automotive industries [47]. The chemical and physical properties of platinum are shown in Table1.3

Platinum nanoparticles are usually in the form of a suspension or colloid of sub-micrometre-sized particles of platinum in a fluid, usually water. A colloid is technically defined as a stable dispersion of particles in a fluid medium (liquid or gas). It can be made with sizes between about 2 and 20 nm, depending on reaction

conditions. Trillions of platinum nanoparticles are suspended in the brownish red or black colored colloidal solution. Nanoparticles come in wide variety of shapes rods, cubes and tetrahedra [48].

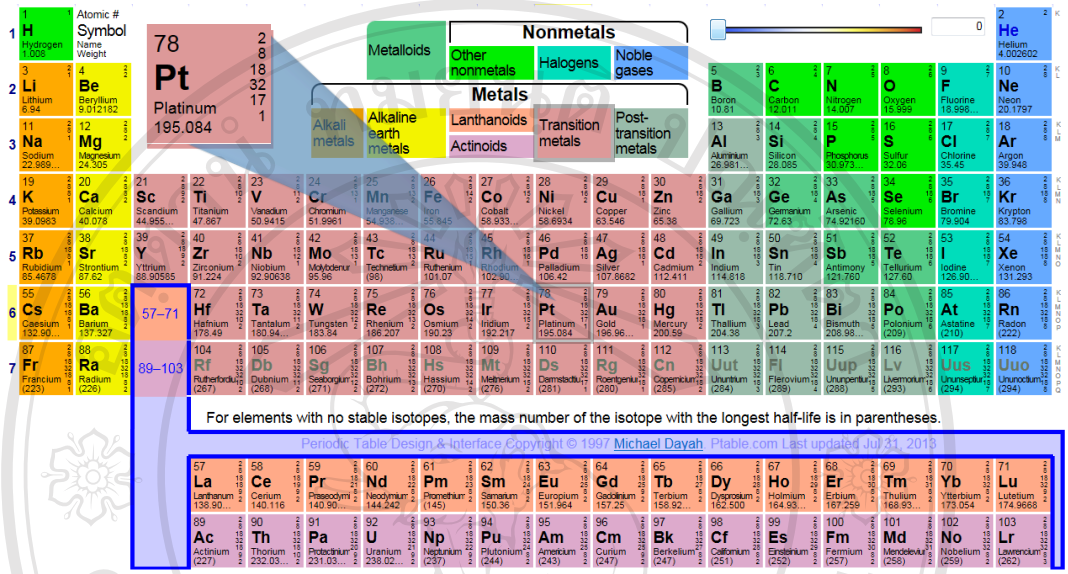

Figure 1.2 The periodic table of Pt element [49].

Table 1.2 Chemical and physical properties of Pt [46].

Property	Value
Stand atomic weight	195.084
Phase	Solid
Liquid density of melting point	21.45 g·cm^{-3}
Melting point	1,768 ^{o}C
Boiling point	3,825 ^{o}C
Heat of fusion	22.17 kJ·mol^{-1}
Heat of vaporization	469 kJ·mol^{-1}
Molar heat capacity	25.86 J·mol^{-1}·K^{-1}
Crystal structure	Face-centered cubic
Electrical resistivity	(20 ^{o}C) 105 nΩ·m
Thermal conductivity	71.6 W·m^{-1}·K^{-1}

1.4 Gold (Au) [50–51]

Gold is a chemical element with the symbol Au and atomic number 79 as shown in the Figure 1.3. It is a dense, soft, malleable, and ductile metal with a bright yellow color and luster that is considered attractive, which is maintained without tarnishing in air or water. Chemically, gold is a transition metal and a group 11 element. It is one of the least reactive chemical elements, solid under standard conditions. The metal therefore occurs often in free elemental (native) form, as nuggets or grains in rocks, in veins and in alluvial deposits. Less commonly, it occurs in minerals as gold compounds, usually with tellurium [50]. The chemical and physical properties of gold are shown in Table1.3.

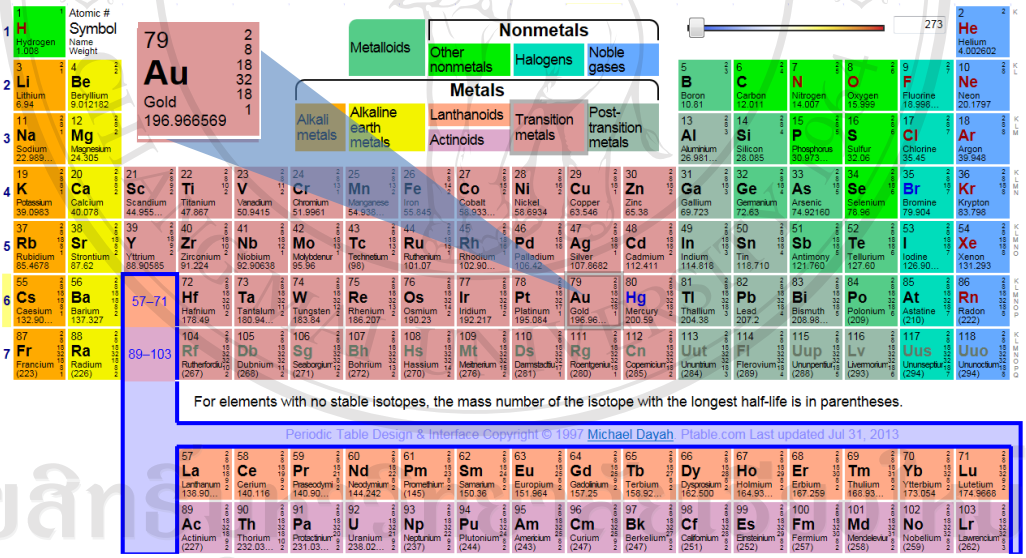

Figure 1.3 The periodic table of Au element [49].

In any application of gold nanoparticles, it is important first to determine their basic physico-chemical characteristics, such as e.g. size, shape, mono- or polydispersity, UV–vis and other spectral properties, electrokinetic potential and some other special parameters [51]. Due to the unique optical, they are the subject of

substantial research, with applications in a wide variety of areas, including electron microscopy, electronics, nanotechnology and materials science.

Table 1.3 Chemical and physical properties of Au [50].

Property	Value
Stand atomic weight	196.9665
Phase	Solid
Liquid density of melting point	17.31 $g \cdot cm^{-3}$
Melting point	11,947 ^{o}C
Boiling point	5,173 ^{o}C
Heat of fusion	12.55 $kJ \cdot mol^{-1}$
Heat of vaporization	324 $kJ \cdot mol^{-1}$
Molar heat capacity	25.418 $J \cdot mol^{-1} \cdot K^{-1}$
Crystal structure	lattice face centered cubic
Electrical resistivity	(20 ^{o}C) 22.14 $n\Omega \cdot m$
Thermal conductivity	71.6 $W \cdot m^{-1} \cdot K^{-1}$

1.5 Silver (Ag) [52–53]

Silver is a chemical element with the chemical symbol Ag and atomic number 47. A soft, white, lustrous transition metal, it possesses the highest electrical conductivity of any element and the highest thermal conductivity of any metal. The metal occurs naturally in its pure, free form (native silver), as an alloy with gold and other metals, and in minerals such as argentite and chlorargyrite. Most silver is produced as a byproduct of copper, gold, lead, and zinc refining [52]. The chemical and physical properties of gold are shown in Table1.4.

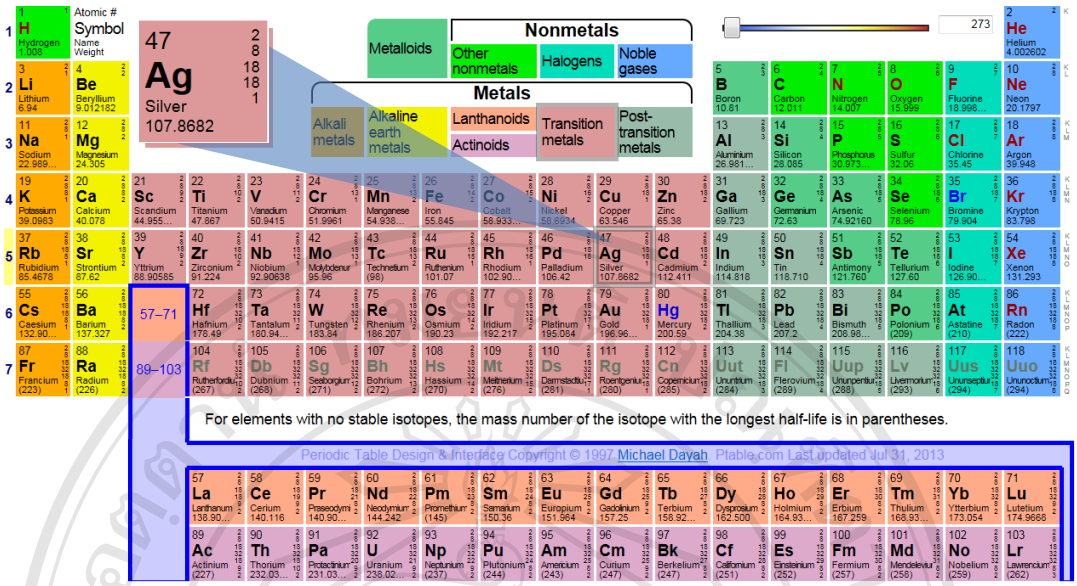

Figure 1.4 The periodic table of Ag element [49].

Table 1.4 Chemical and physical properties of Ag [52].

Property	Value
Stand atomic weight	107.8682
Phase	Solid
Liquid density of melting point	9.320 $g \cdot cm^{-3}$
Melting point	961.78 ºC
Boiling point	2,162 ºC
Heat of fusion	11.28 $kJ \cdot mol^{-1}$
Heat of vaporization	250.58 $kJ \cdot mol^{-1}$
Molar heat capacity	25.350 $J \cdot mol^{-1} \cdot K^{-1}$
Crystal structure	face centered cubic
Electrical resistivity	(20 ºC) 22.87 nΩ·m
Thermal conductivity	429 $W \cdot m^{-1} \cdot K^{-1}$

In recent years, silver nanoparticles have drawn a lot of attention due to their unusual physical and chemical properties, which largely differ from their bulk properties. They shows unique properties such as excellent conductivity, chemical stability, and catalytic activity, etc. which are dependent on the particle size, size

distribution and shape. Among all metals, silver has the highest electrical and thermal conductivity. Silver materials with zero-, one-, or two-dimensional nanostructures such as nanoparticles, nanowires, and nanocubes are believed to have great potential for applications in optics, catalysis, and other fields. In the characteristic of silver material, the low sintering temperature of silver nanoparticles is important in flexible electronic applications [53].

1.6 Flame spray pyrolysis [54–58]

Flame spray pyrolysis (FSP) is such a simple combustion synthesis process where a metal-containing precursor solution is injected and atomized into a flame [54] such as carbon blacks, fumed SiO_2 and TiO_2 and to a lesser extent, for specialty chemicals such as Al_2O_3 and ZnO powders [55]. However, by using a vapor-fed flame reactor it is often difficult to produce multicomponent materials with homogeneous chemical composition because differences in the chemical reaction rate and the vapor pressure of the reactants, nucleation and growth rates of the product may lead to nonuniform composition from particle to particle or even within a single particle. Therefore, flame spray pyrolysis (FSP) processes are quite attractive as they can employ a wide array of precursors for synthesis of a broad spectrum of functional nanoparticles e.g. ceria for catalysts or chemical mechanical polishing and laser diodes as each droplet contains the precursor in the same stoichiometry as desired in the product [56]. Flame aerosol synthesis is a cost-effective and versatile process for controlled production of nanoparticles [55]. The basic steps of particle formation and growth by gas-to-particle conversion in flame spray pyrolysis were shown in Figure 1.5.

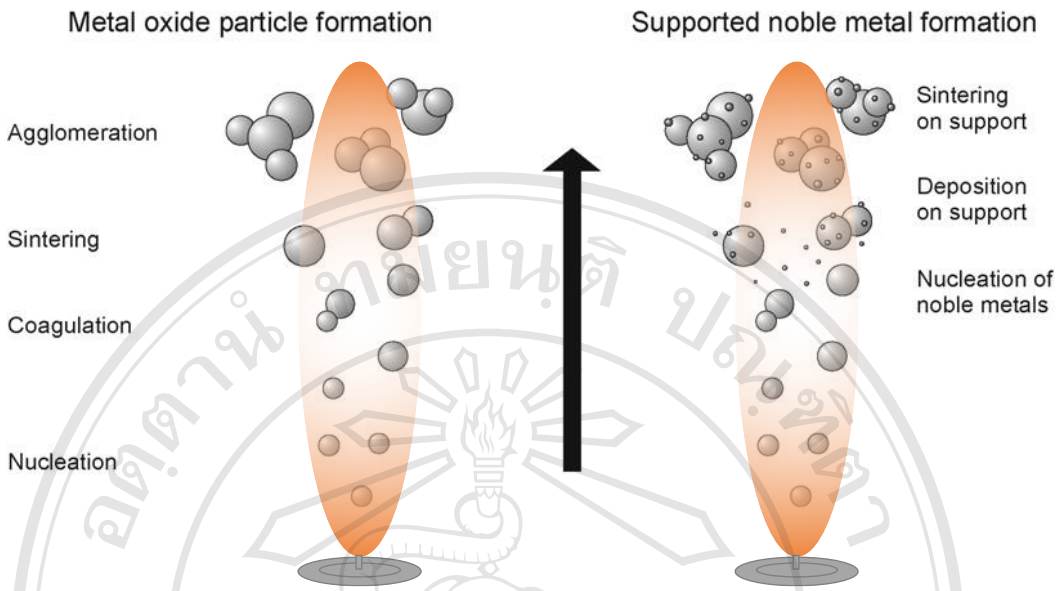

Figure 1.5 Formation of nanoparticles in flames. After evaporation and combustion of the precursors, particle formation starts by nucleation from the gas phase. These particles coagulate and, depending on the temperature, sinter into larger particles or agglomerate. In the case of supported noble metal catalysts, noble metal particle formation starts after support formation by homogeneous nucleation from the gas phase and/or heterogeneous nucleation on the support [57].

Moreover, at low oxidant flow rates, the specific surface area increased with increasing oxidant flow rate as the spray flame length was reduced, leading to shorter resident time and allowing less time for particle growth. Using pure oxygen as oxidant the droplets burn much faster than with air, thus, product particles experience longer resident times at higher temperature [58]. The effect of solution feed rate on particles specific surface area and crystalline size was also investigated [58]. The solution feed rate increased the flame height, and therefore coalescence was enhanced, resulting in larger primary particles [58].

Supported noble metals are widely used as catalysts in processes ranging from fine chemical synthesis to exhaust gas treatment and even oil refining. Small active metal clusters are generally dispersed on high surface area supports such as TiO_2, Al_2O_3 and SiO_2. Various flame techniques have been applied for preparation of supported noble metal catalysts in one step, although FSP is the dominant technique as it allows high throughput of the noble metal. The relatively high vapor pressure of noble metals compared to that of the supporting metal oxides allows the cosynthesis of support with the noble metal. In a first step, the support is formed and then downstream noble metal particles nucleate at lower temperatures either heterogeneously on the support or homogeneously in the gas phase with later deposition on the support [57].

1.7 Characterization techniques

1.7.1 X-ray diffraction method [59–65]

X-ray diffraction (XRD) technique is a standard tool for identification of crystalline phases in powder samples. This technique is based on the elastic X-rays scattering from structures and the radiation wavelength is approximately about 1 Å, which is about the same size as an atom. X-rays radiations occur in the portion of electromagnetic spectrum between gamma-rays and the ultraviolet. When X-rays hit with a crystalline substance, the X-ray diffraction pattern can be obtained. Each crystalline solid has its unique characteristic X-ray powder pattern which is employed to study for its identification. The crystalline phase in the sample diffracts X-rays according to Bragg's equation which relates lattice spacing to the wavelength of the X-rays. The amount of sample needed in practice is roughly 100 mg or more.

Crystalline phases present at the levels of about 1 percent or greater can be detected. The unit cell dimension (a, b, c) of the crystal can also be determined and provide more information for complex structure materials. Amorphous materials are not observed. In routine work, XRD relies on availability of standards that allow identification of peaks in the diffraction pattern.

Bragg law, formulated by Bragg *et al.*[59] in 1913, relates the wavelength of the X-rays to the spacing of the atomic planes. Consider the diffracted wave in Figures 1.6. It is assumed to make the same angle, θ, with the atomic planes as does the incident wave. The criterion for the existence of the diffracted wave is that the scattered (reflected) X-ray should all be in phase across a wave front. This turns out to be a real convenience, so we set $d = d'/n$ and write the Bragg law in the form

$$n\lambda = 2d \sin\theta \qquad (1.1)$$

where λ = wavelength of the X-ray,

d = interplanar spacing of the crystal,

θ = angle between the lattice plane and the X-ray,

n = an integer

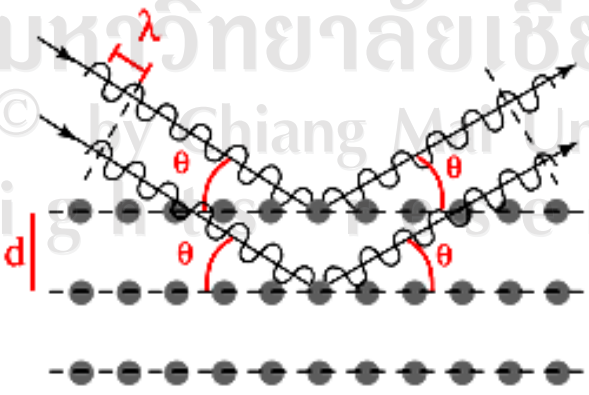

Figure 1.6 Diffraction of X-rays by a crystal [65].

The scattering of electrons, X-rays and neutrons by crystals can be described as a reflection of the beams at planes of atoms (lattice planes), independent of the actual physical reason causing the diffraction event. If the incident plane wave hits the crystal at an arbitrary angle, the interference of the reflected waves can be either destructive or constructive. To obtain constructive interference, the path difference between the two incident and the scattered waves, which is $2d\sin\theta$, has to be a multiple of the wavelength λ. For this case, the Bragg law then gives the relation between interplanar distance d and diffraction angle θ

1.7.2 Scanning Electron Microscopy (SEM) [55, 58, 66−69]

In a scanning electron microscope, a tiny electron beam is scanned across the sample. Schematic diagram of a scanning electron microscope was shown in Figure 1.7. Simultaneously, the generated signals are being recorded, and an image is formed pixel by pixel. In SEM, the signals are observed on the same specimen site as the incoming electron beam (cf. STEM, using transmitted electrons). In contrast to TEM methods needing very thin samples, compact samples can thus be investigated by SEM. Valuable information about morphology, surface topology and composition can be obtained. SEM microscopes achieving resolutions below 1 nm are available now. The resolution of a typical SEM is about 0.01 μm, not as good as a TEM but much better than an optical microscope and adequate for most particle studies. Like the TEM, the SEM is limited to solid, nonvolatile particles. Unlike the TEM, the electron beam does not have to penetrate the sample support, so SEM samples are usually mounted on the end of an aluminum cylinder 1–3 cm in diameter. Precautions must be taken to prevent the buildup of electric charge on the sample surface, which would

deflect the electron beam and cause distortion of the image and particle loss by electrostatic repulsion. This is usually done by applying a very thin (< 0.01 μm) coating of gold or carbon to the surface of the particle with a sputter–coating apparatus. Particles can be deposited onto any surface that can be attached to the sample cylinder and made conductive. The smooth surface of a Nuclepore filter provides a suitable surface for viewing particles, and particles larger than its pore size can be sampled directly onto the filter surface. Scanning electron microscopes have a depth of field that is over 300 times greater than that of optical microscopes and a wide range of magnifications, 20–100,000X. For particle evaluation, a magnification range of 100–10,000X is most commonly employed. The great depth of field and the accurate rendition of surface features make the SEM well suited to particle sizing and morphology studies. A scanning electron microscope can be employed as a microprobe to determine elemental composition of particles. The electron beam is held fixed on a particle and the X-rays emitted are detected by a solid state X-rays is related to the Z number of the elements in the particle and provides an elemental analysis of the particles for Z > 12. Although less common, an Auger electron velocity analyte can be used in the same way to determine elemental composition for Z < 20. The adjustable electron beam voltage of 1–30 kV facilitates these analyses.

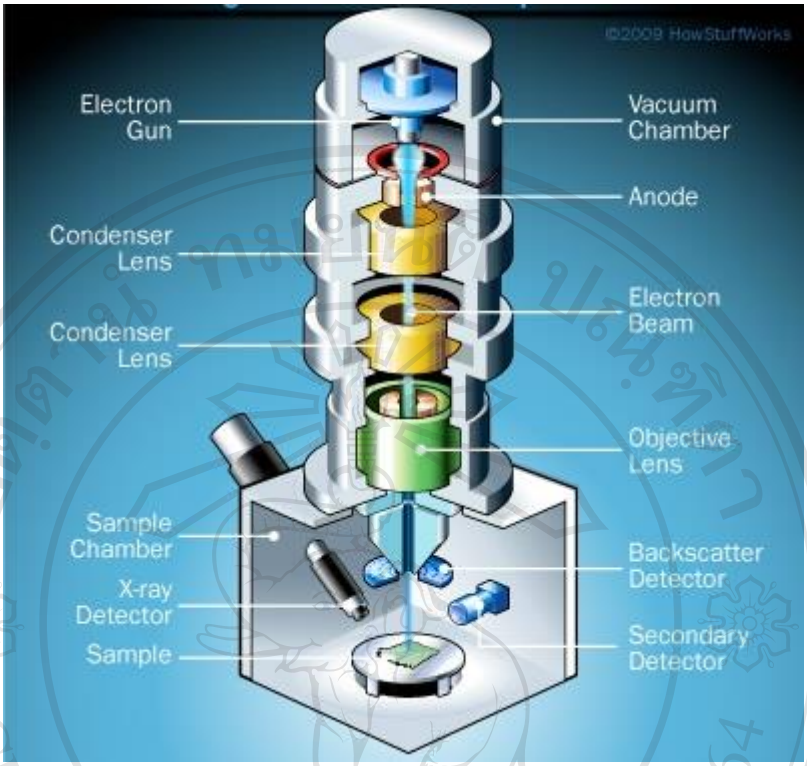

Figure 1.7 A schematic drawing of a SEM microscope including the interactions between a bulk specimen and the incident e-beam [69].

Figure 1.7 shows a schematic drawing of a SEM microscope including the interactions between a bulk specimen and the incident e-beam which can be described as follows [58]:

- At the top of the picture is an electron gun, producing a stream of monochoromatic electrons.
- The electron beam is condensed by the first condenser lens, which is used to form the beam. Together with the condenser aperture it eliminates the high-angle electrons from the beam.

- The second condenser lens forms the electrons into a thin, tight, coherent beam and is usually controlled by the “fine probe current”.
- A user selectable objective aperture further eliminates high-angle electrons from the beam.
- A set of coils then “scan” or sweep” the beam in a grid fashion like a television, dwelling on points for a period of time (usually in the microsecond range) determined by the scan speed.
- The final lens, the objective lens, focuses the scanning beam onto the desired part of the specimen.
- When the beam strikes the sample interactions occur inside the sample and are detected with various instruments.
- Before the beam moves to its next dwell point these detectors count the number of interactions and display a pixel on a screen whose intensity is determined by this number. Generally, the more reactions the brighter the pixel.
- This process is repeated until the grid scan is finished and then repeated.

1.7.3 Transmission Electron Microscopy (TEM) [42, 70−74]

Transmission electron microscope (TEM), electrons are transmitted through the sample. Normally the incident and scattered electrons are referred to as electron beams. In TEM, the electron beam is transmitted through the instrument’s optics. The

TEM has an electron gun and electromagnetic lenses which include condenser and objective lenses. The condenser lenses converge and control the electron beam and illuminate the sample, and the objective lenses forms the image of the sample and diffraction. The images and diffractions are then magnified by other lenses in the system. A base reference line passing through the center of all the lenses is called the optic axis of the electron. A typical, TEM working is shown in Figure 1.8.

The capabilities of the TEM are that particles can be studied in morphology (size, shape and particle arrangement), crystallographic (atom arrangement, atomic-scale defects) and compositional information. Due to the using of electrons source, a high resolution can be obtained since they have both of low wavelength and particle properties, that means a beam of electrons behaves like a beam of radiation, yet they can still interact with the sample because of their electrical charge. Moreover, this technique is particularly important in the study of crystal line structure, known as high resolution electron microscopy (HRTEM). Due to the difference in phase of electron waves scattered through the sample, the phase contrast imaging as the images are formed. The possibility for high magnification has made both of TEM and HRTEM as primary useful tools for a number of researches.

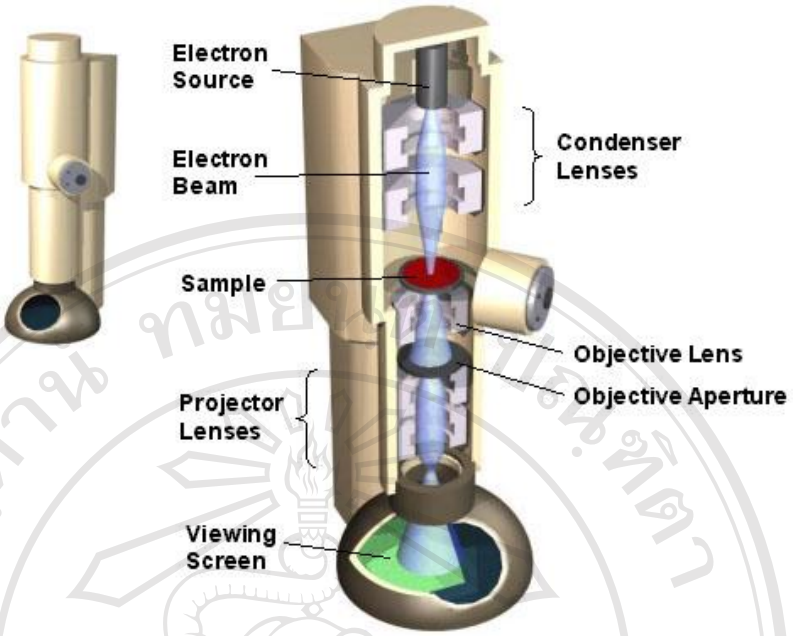

Figure 1.8 A schematic drawing of the interactions between an electron transparent specimen and the incident e-beam in a TEM [74].

Figure 1.8 a schematic drawing of the interactions between an electron transparent specimen and the incident e-beam in a TEM which can be described as follows [73]:

- The electron gun, produces a coherent monochromatic electron beam, as in the case of SEM.
- This beam is focused by the use of condenser lenses 1 and 2. The first lens largely determines the “spot size”; the general size range of the final spot that strikes the sample. The second lens changes the size of the spot on the sample; changing it from a wide dispersed spot to a pinpoint beam.
- The beam is restricted by the condenser aperture, to filter high angel electrons.

- The beam strikes the specimen and parts of it are transmitted.
- The objective lens is the most critical lens since it determines the resolving power of the instrument and performs the first stage of imaging. The objective aperture is positioned in the back focal plane of the objective lens, where electron diffraction patterns are formed, and limits the electron beams contributing to the final image. The selected area electron diffraction aperture can select the area of interest in order to obtain the diffraction pattern of that region.
- The image is passed down the column through the intermediate and projector lenses, being enlarged all the way.
- The image strikes the phosphor image screen and light is generated, allowing the user to see the image. The darker areas of the image represent those areas of the sample through which fewer electrons were transmitted (thicker or denser part of the sample).

1.7.4 The Brunauer-Emmett-Teller (BET) [75, 76]

BET theory is a well-known rule for the physical adsorption of gas molecules on a solid surface. The Brunauer-Emmett-Teller method is based on non-specific physisorption of a gas (N_2 or Ar) onto a solid close to the condensation temperature of the adsorbing gas. Estimates of surface areas provide information about the porosity of particles and the primary particle size in particles that consist of agglomerates of smaller particles. The primary particle size can be related to surface area assuming

that the particles are smooth monodisperse spheres. Specific surface areas can range from a few m^2/g to hundreds of m^2/g in the case of highly porous materials or very fine particles. Adsorption is characterized by an isotherm which represents the equilibrium amount of gas adsorbed on a solid at a given temperature as a function of pressure.

The BET method is widely used in surface science for the calculation of surface areas of solids by physical adsorption of gas molecules. A total surface area S_{total} and a specific surface area S are evaluated by the following equations:

$$S_{total} = \frac{V_m \overline{N} \mathscr{A}}{\overline{M}} \quad (1.2)$$

Where:

S_{total} is sample surface area

$\mathscr{A}$ is the cross-sectional area

$\overline{M}$ is the molecular weight of an adsorbate molecule

$\overline{N}$ is the Avogadro's number

The particle size (d_{BET}) is calculated by BET measurement using specific surface area (SSA) and density of sample by assuming that the particles do have spherical shape. The following equation can be used:

$$d_{BET} = \frac{6}{SSA_{BET}\rho_{sample}} \quad (1.3)$$

Where: ρ_{sample} is the density of the sample

1.8 Semiconductor gas sensors [55, 77–92]

Many metal oxides are suitable for detecting combustible, reducing, or oxidizing gases by conductive measurements. The following oxides show a gas response in their conductivity: Cr_2O_3, Mn_2O_3, Co_3O_4, NiO, CuO, SrO, In_2O_3, WO_3, TiO_2, V_2O_3, Fe_2O_3, GeO_2, Nb_2O_5, MoO_3, Ta_2O_5, La_2O_3, CeO_2, Nd_2O_3 [77]. Metal oxides selected for gas sensors can be determined from their electronic structure. The range of electronic structures of oxides is so wide that metal oxides were divided into two the following categories [78]:

(1) Transition-metal oxides (Fe_2O_3, NiO, Cr_2O_3, *etc.*)

(2) Non-transition-metal oxides, which include (a) pre-transition-metal oxides (Al_2O_3, *etc.*) and (b) post-transition-metal oxides (ZnO, SnO_2, *etc.*).

Pre-transition-metal oxides (MgO, *etc.*) are expected to be quite inert, because they have large band gaps. Neither electrons nor holes can easily be formed. They are seldom selected as gas sensor materials due to their difficulties in electrical conductivity measurements. Transition-metal oxides behave differently because the energy difference between a cation d^n configuration and either a d^{n+1} or d^{n-1} configurations is often rather small [79]. They can change forms in several different kinds of oxides. So, they are more sensitive than pre-transition-metal oxides to the environment. However, structure instability and non-optimality of other parameters important for conductometric gas sensors limit their field of applications. Only transition-metal oxides with d^0 and d^{10} electronic configurations find their real gas sensor application. The d^0 configuration is found in binary transition-metal oxides such as TiO_2, V_2O_5, WO_3. d^{10} configuration is found in post-transition-metal oxides, such as ZnO, SnO_2 [80].

Gases are the key measure in many industrial and domestic activities. Detection of pollutant, toxic, refining, combustible and process gases is important for system and process control, safety monitoring and environmental protection. In the last decade the specific demand for gas detection and monitoring has emerged particularly as the awareness of the need to protect the environment has grown. Chemical sensors with metal oxides as sensing material have been around for a long time as a low cost alternative for gas detection devices. However, they have, to some extent, suffered from limitations in sensitivity, selectivity and stability when compared to more expensive alternatives. Recent advances in nanotechnology and nanomaterials have fostered fabrication techniques that can be harnessed to increase the response and performance of these materials. This is because their performance is governed by the exposed surface area; the gas sensing mechanism being due to reactions that occur at the sensor surface. Better adsorption-desorption phenomena on higher surface area would enhance the sensitivity of gas sensor. Therefore, gas sensor based on nanostructured materials should be able to detect sensing gas molecules at lower concentration and present better sensing properties than gas sensors based on bulk materials [81–84].

Usually the devices for laboratory tests are furnished with a heater so that they are heated externally to obtain an optimum operating temperature. Upon exposure to a particular gas (target gas) of a low concentration in air, the sensor changes its electrical resistance. The resistance change is caused by a loss or a gain of surface electrons as a result of adsorbed oxygen reacting with the target gas. If the oxide is an n-type, there is either a donation (reducing gas) or subtraction (oxidizing gas) of electrons from the conduction band. The result is that n-type oxides increase their

resistance when oxidizing gases such as NO_2, O_3 are present while reducing gases such as CO, CH_4, C_2H_5OH, H_2, SO_2, NH_3, acetone lead to a reduction in resistance. The converse is true for p-type oxides, such as Cr_2TiO_3 [85]. The sensitivity of n-type semiconductor gas sensor for reducing gases and oxidizing gases are shown in equations 1.4 and 1.5, respectively. For p-type semiconductor gas sensor, the definitions are reversed. The gas-sensing sensitivity was calculated from dynamic variation of the conductance due to gas pulses introduction and plotted versus various parameters including temperature and gas concentration [86–90].

$$S = \frac{R_a}{R_g}, S = \frac{R_a - R_g}{R_g} \quad \text{(for reducing gas)} \tag{1.4}$$

$$S = \frac{R_g}{R_a}, S = \frac{R_g - R_a}{R_a} \quad \text{(for oxidizing gas)} \tag{1.5}$$

With chemical sensor, the result usually shows the change in resistance lead to the sensing performance. The sensitivity (or sensor signal, sensor response), S is defined (Figure 1.11) as the several ratios depending on the types of a semiconductor, and the types of the analyte gases, where R_a is the resistance in dry air, R_g is the resistance in test gas.

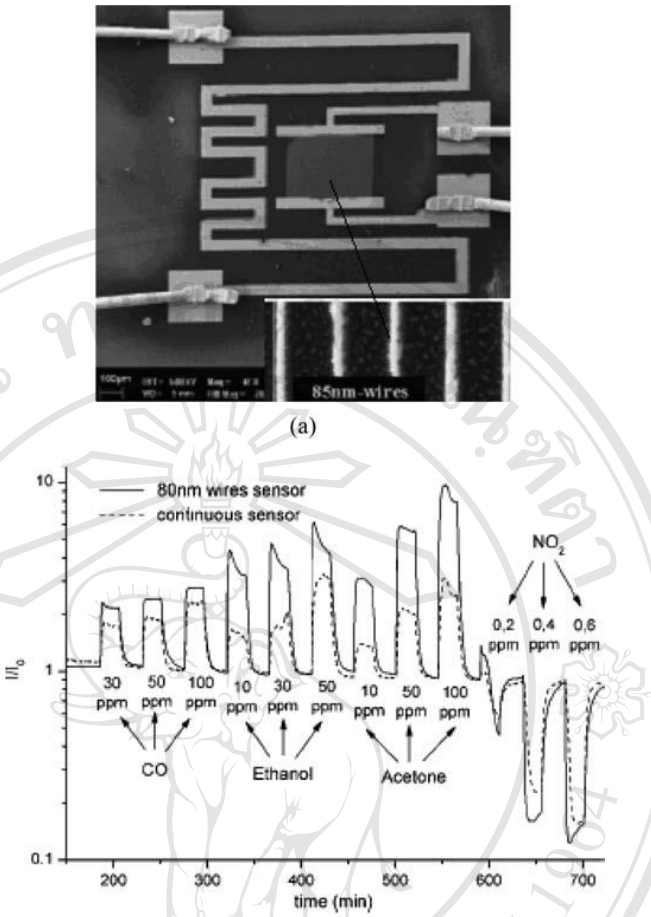

Figure 1.9 (a) Nanowire-pattern sensor device completed with circuitry elements; the nanowire pattern is in the middle of the sample (high magnification in right bottom), whereas all around are the visible heater element and parallel electrode contacts for SnO_2 nanowires. (b) Functional characterization of 80 nm wire-pattern sensor (solid line) and continuous film sensor (dotted line) [91].

The selectivity can be defined as the ability of a sensor to respond primarily to only on species in the presence of other species. This is the most important characteristic of sensors; the ability to discriminate between different substances. Such behavior is principally a function of the selective component, although sometimes the operation of the transducer contributes to the selectivity. This factor is

the essence of sensors. It is the rate to find a sensor which will respond to only one analyte, although some do exist. It is more usual to find a sensor that will respond mainly to one analyte, with a limited response to other similar analyte. Alternately, the response may be to a group of analytes of similar chemical structure, such as carbonyl compounds.

Very much related to the response time is the recovery time. The recovery time is the time that elapses before a sensor is ready to be used for another sample measurement. The resulting response time may be immediate or it may be that after one measurement the sensor system has to rest the resume its base equilibrium before it can be used with the next sample. In many publications, these times are combined and the result is given as the number of samples that can be analyzed per hour, which obviously is the main practical point at the end. Manufacturers typically define some length of time, such as 10 min, as the point at which a sensor reaches its maximum output. A sensor's T_{90} is the times to reach 90% variation in resistance upon exposure to gas and air were defined as the 90% response time ($T_{90\%}$(air-to-gas)) and 90% recovery time ($T_{90\%}$(gas-to-air)), respectively (Figure 1.12). The response and recovery time of n-type semiconductor for reducing gas can be calculated (Equations 1.6 and 1.7) as follows:

$$T_{res} = \left[T_{R_o} - \left\{ \left(T_{R_o} - T_{R_g} \right) \right\} x \frac{90}{100} \right] - T_{R_o} \quad (1.6)$$

$$T_{rec} = \left[T_{R_g} - \left\{ \left(T_{R_o} - T_{R_g} \right) \right\} x \frac{90}{100} \right] - T_{R_g} \quad (1.7)$$

where T_{Ro} is defined the as the time (s) at the baseline resistance in dry air (R_a) and T_{Rg} is denoted as the time (s) at the resistance in test gas (R_g) [55, 85]**.**

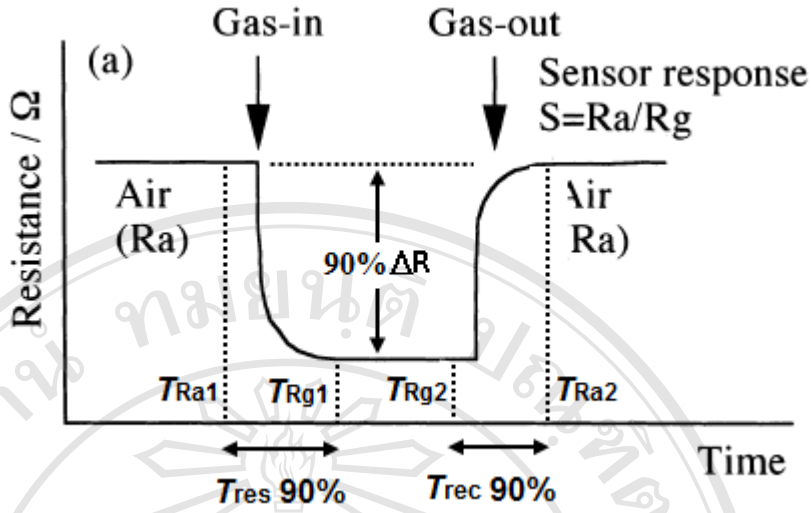

Figure 1.10 The response and recovery time of n-type semiconductor for reducing gas [92].

Stability is often given limited attention in tin oxide sensor development studies although it is a key quality indicator for gas detection. There are numerous studies in the literature on improving sensitivity and selectivity, but few studies supply stability data. The success of a sensor will be limited if the sensor performance is not demonstrated as repeatable and stable over long-term testing. Problems of stability, as outlined by Park and Akbar [93], may be attributed to three primary areas of concern. The first is that a surface conductive sensor can suffer from surface contamination. Second, changes in the sensor characteristics (such as intergranular connectivity) can occur due to thermal expansion coefficient mismatch and/or interfacial reactions at the metal electrode/ceramic interface. Lastly, the film morphology may change over time due to the relatively high operating temperatures of the sensor, which may also cause migration of additives [94].

1.8.1 Gas sensing mechanism [95–108]

Metal oxide is an *n*-type semiconductor, where the sensor conductivity increase in the presence of a reducing gases, and decrease in the presence of an oxidizing gas. Metal oxide sensor response is due to surface interactions between the metal oxide and the surrounding gases. The general steps involved in sensor response upon exposure to air and to a reducing gas, R, are shown in Figure 1.13. As shown in the Figure 1.13, oxygen from the air is adsorbed onto the surface of the metal oxide. Electrons from the surface region of the metal oxide are transferred to the adsorbed oxygen, leading to the formation of an electron-depleted region near the surface of the metal oxide particle. The electron depleted region, also called the space-charge layer, is an area of high resistance and the core region of the particle, where electron densities are high, is an area of relatively low resistance.

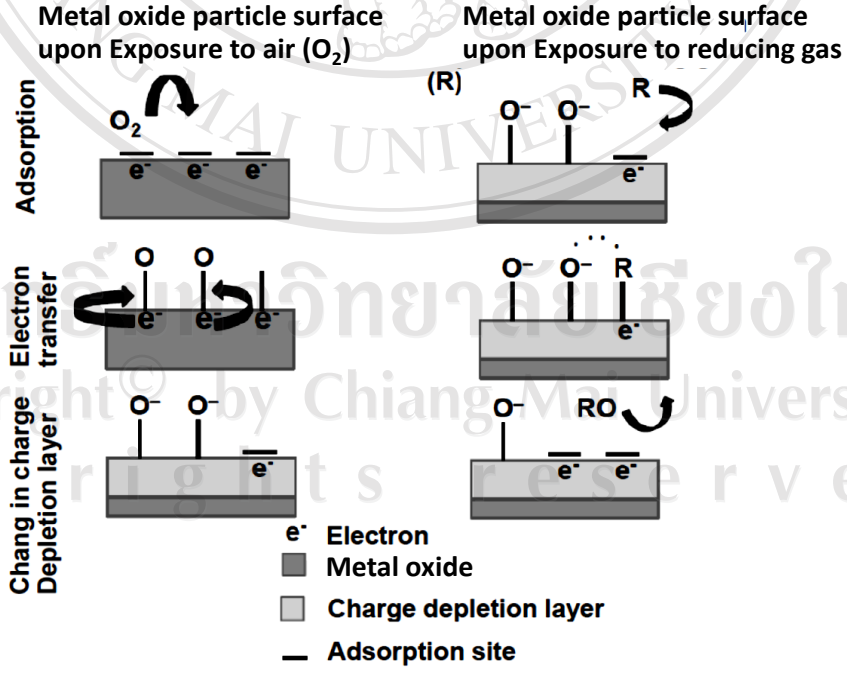

Figure 1.11 Schematics indicating the mechanisms leading to metal oxide sensor response to oxidizing and reducing gases [95].

The form of the adsorbed oxygen (either molecular or atomic) depends on the temperature of the sensor, where O_2^- species have been observed at lower temperatures (below 200°C) and O^- or O^{2-} species have been observed at higher temperature (above 200°C) [94]. The process can be expressed in the following reactions [97]:

$$O_2\,(\text{gas}) \rightarrow O_2\,(\text{absorbed}) \quad (1.8)$$

$$O_2\,(\text{absorbed}) + e^- \rightarrow O_2^-\,(\text{adsorbed}) \quad (1.9)$$

$$O_2^-\,(\text{adsorbed}) + e^- \rightarrow 2O^-\,(\text{adsorbed}) \quad (1.10)$$

$$O^-\,(\text{adsorbed}) + e^- \rightarrow O^{2-}\,(\text{adsorbed}) \quad (1.11)$$

When metal oxide surfaces are exposed to oxidizing gas such as NO_2, this gas react with the adsorbed O^- ions as well as adsorb directly on the surface of metal oxide surface. The oxidizing reactions between metal oxide and NO_2 gas follow the reaction paths [98]:

$$NO_2\,(g) + e^- \leftrightarrow NO_2^-\,(ads) \quad (1.12)$$

$$NO_2\,(g) + e^- \leftrightarrow NO(g) + O^-\,(ads) \quad (1.13)$$

And then the metal oxide surface is exposed to reducing gases, the gas reacts with the chemisorbed oxygen thereby releasing electrons back to the conduction band. The overall reducing reactions between NH_3, H_2S, CO, SO_2 CH_4, H_2, C_2H_2 and C_2H_5OH gases, and the chemisorbed oxygen species (O^- and O^{2-}) are given by [99–108]:

$$2NH_3 + 3O^-\,(\text{ads}) \rightarrow N_2 + 3H_2O + 3e^- \quad (1.14)$$

$$2NH_3 + 3O^{2-}\,(\text{ads}) \rightarrow N_2 + 3H_2O + 6e^- \quad (1.15)$$

$$H_2S + 3O^-\,(\text{ads}) \rightarrow H_2O + SO_2 + 3e^- \quad (1.16)$$

$$H_2S + 3O^{2-}(\text{ads}) \rightarrow H_2O + SO_2 + 6e^- \quad (1.17)$$

$$CO + O^-(\text{ads}) \rightarrow CO_2 + e^- \quad (1.18)$$

$$CO + O^{2-}(\text{ads}) \rightarrow CO_2 + 2e^- \quad (1.19)$$

$$SO_2 + O^-(\text{ads}) \rightarrow SO_3 + e^- \quad (1.20)$$

$$SO_2 + O^{2-}(\text{ads}) \rightarrow SO_3 + 2e^- \quad (1.21)$$

$$CH_4 + 4O^-(\text{ads}) \rightarrow 2H_2O + CO_2 + 4e^- \quad (1.22)$$

$$CH_4 + 4O^{2-}(\text{ads}) \rightarrow 2H_2O + CO_2 + 8e^- \quad (1.23)$$

$$H_2 + O^-(\text{ads}) \rightarrow H_2O + e^- \quad (1.24)$$

$$H_2 + O^{2-}(\text{ads}) \rightarrow H_2O + 2e^- \quad (1.25)$$

$$C_2H_2 + O^-(\text{ads}) \rightarrow H_2O + 2C + e^- \quad (1.26)$$

$$C_2H_5OH\ (\text{gas}) + O^- \Leftrightarrow CH_3CHO + H_2O + e^- \quad (1.27)$$

$$C_2H_5OH\ (\text{gas}) \Leftrightarrow H + C_2H_5O\ (\text{surface}) \quad (1.28)$$

$$C_2H_5O \rightarrow H + CH_3CHO \quad (1.29)$$

$$CH_3CHO + O\ (\text{bulk}) \rightarrow CH_3COOH + O\ (\text{vacancies}) \quad (1.30)$$

1.8.2 Catalytic additives on semiconducting oxide sensors [80, 87, 96, 109–114]

The addition of an appropriate amount of metal additives has been shown to improve the detection of various kinds of gases via the enhancement of the sensor response and a decrease of the temperature of maximum sensor response. A decrease in response time and better selectivity are also claimed to be achievable by using these additives.

The use of additives on semiconducting oxides is evidently related to the use of supported metal/semiconducting oxide in catalysis. In this field, the main target is to enhance the reaction rate of the gases. On the other hand, in the field of semiconducting oxide sensors, this higher rate of reaction must be translated into an electrical signal; otherwise no advantage for gas sensing is taken from catalyzing the reaction.

It is accepted that metal additives can lead to two different sensitization mechanisms: chemical sensitization and electronic sensitization [110]. In the first case, the promoting effect is due to the ability of noble metal to activate inflammable gases by enhancing their spill-over, so that they react with oxygen adsorbates more easily. Besides, the supply of oxygen can be enhanced by the presence of these catalytic additives, at the surface of which oxygen molecules from the gas phase can be easily dissociated and oxygen atoms migrate through spill-over effect to the surface of the semiconducting oxide. In this way, the additive exerts a sort of remote control on the catalytic and sensing properties of the semiconducting oxide.

On the other hand, the electronic sensitization is associated with oxidized metal additives. The addition of fine particles of some metals to n-type metal oxides usually results in a rise of the base resistance in air. There is a decrease in the electron concentration in the oxide surface layer, which corresponds to an increase of the space-charge depth as a result of the electron transfer from the metal oxide to the metal loaded onto its surface. When the metal surface is covered with oxygen adsorbates at elevated temperatures in air (i.e. the metal is oxidized), the oxygen adsorbates extract electrons from this metal, which in turn extracts electrons from the metal oxide, leading to a further increase in the space-charge depth. Consumption of

oxygen adsorbates on the metal, in addition to those on the semiconducting oxide surface, by reaction with flammable gases, causes the enhanced sensitivity. In this case, therefore, the promoting effect arises mainly from the change in the oxidation state of the loaded material.

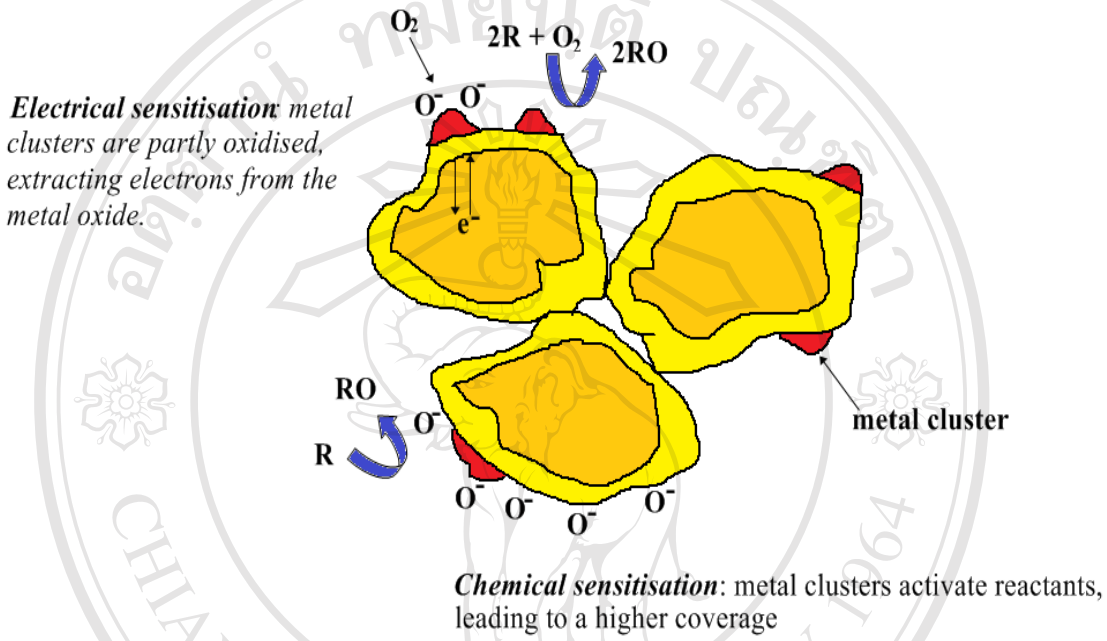

Figure 1.12 Catalytic additives on semiconducting oxide sensors. Top: Electrical sensitization - oxidation state of metallic clusters depend on ambient gases. Bottom: Chemical sensitization - metallic clusters promote the activation of gaseous specie [90, 96, 109].

Commonly, two concepts are invoked to explain the improvement of the nanowire's sensing performance upon metal deposition. One is the "electronic mechanism" proposal and the other is a "chemical" process. The "electronic mechanism" considered that depletion zones formed around the modified particles (Figure 1.15b) and the modulation of the nano-Schottky barriers (and hence the width of the conduction channel) which is due to changes in the oxidation state of the metal

accompanying oxygen adsorption and desorption is responsible for the sensing enhancement. However, the “electronic mechanism” has some difficulties in explaining the kinetics and temperature dependence brought about by metal functionalization, while the “chemical” process not. The latter mechanism bases on the highly effective dissociation catalytic ability of metal. The ionosorption of oxygen at defect sites of the pristine surface is shown in Figure 1.15a process-1. Metal is a far better oxygen dissociation catalyst than tin oxide and catalytically activate the dissociation of molecular oxygen in process one. Then atomic products diffuse to the metal oxide support as shown in Figure 1.15a process-2. Furthermore, it is not necessary for molecular oxygen to dissociate on Pd surface only in process two. It is believed that oxygen molecules can reside briefly on an oxide support and diffuse to a catalyst particle before it has had an opportunity to desorb [111]. This is the so-called “back-spillover effect” (procees-3 in Figure 1.15a).There is an effective “capture radius” (Rc in Figure 1.15b) around the metal particles. An effective oxygen delivery system forms if the whole surface of metal oxide covered by this oxygen “collect zones” [112]. The net results of process-2 and -3 significantly enhance the probability of oxygen ionosorption on metal oxides and hence the sensitivity. The interaction of reducing gas such as H_2, with pristine and metal-functionalized metal oxide was thoroughly discussed in [113] and the principle transduction mechanism is similar to that of O_2 mentioned above. However, the dispersion of catalysts is also an important factor to develop the potential of catalysts. So, the structure of catalyst supporting materials would be considered in the next step [80].

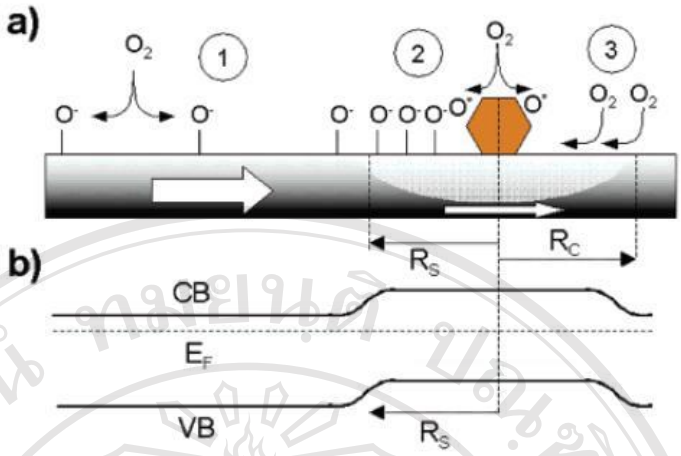

Figure 1.13 (a) Schematic depiction of the major process taking place at a metal oxide nanowire/nanobelt surface when exposed to O_2. (b) Band diagram of the pristine metal oxide nanostructure and in the vicinity (and beneath) a metal oxide nanoparticle. The radius of the depletion region is determined by the radius of the spillover zone (adapted from [114]).

1.9 Literature reviews

Walton *et al*. [115] reported that thin Pt/TiO_{2-x} sensing films were characterized by X-ray photoelectron spectroscopy (XPS) and ultra-violet photoelectron spectroscopy (UPS) to explain the mechanism decreases resistance on exposure to hydrogen and propylene. The Pt/TiO_{2-x} films were prepared by oxidizing Pt/Ti films in 10^{-6} mbar O_2 at 800 to 900 K. The gas sensitivity of the films arose with activation that consisted of a reduction step at 750 K followed by a final oxidation treatment at 900 K. Changes in the film stoichiometry during each of the pretreatment and activation steps could be clearly detected with XPS. The onset of gas sensitivity was attributed to oxidation of the titanium metal and the formation of a discontinuous film structure which was revealed in scanning electron microscopy (SEM) images of

activated Pt/TiO_{2-x} sensing films. Resistance decreases in the range of 1 to 10% were observed for these films following hydrogen or propylene exposure in the 10^{-6} to 10^{-2} mbar range at $T \leq 700$ K. Larger resistance decreases were observed with increasing reducing gas pressure. The resistance decreases were caused by surface reduction at $T \leq 700$ K with increasing sub-surface/bulk oxygen at high temperature. XPS measurements indicated that resistance decreases due to reducing gas exposure at film temperatures ≤ 700 K could be correlated with decreases in the surface oxygen concentration.

Ruiz *et al*. [116] reported that nanocrystalline titanium dioxide after hydrothermal treatment was loaded singly or doubly with various metals or metal oxides (Au, Ag, Pt, Pd, Cu, Co, Nb, V). Hydrothermally treated TiO_2 exhibited enhanced thermal stability as resistance to grain growth and phase transformation. Incorporation of metal additives further decreased the grain size of titania, while the phase transition was generally promoted, except in the case of Au and Pd, where predominant anatase phase was maintained up to 800 ºC. Among the different additives tested, Au was found to be the most attractive promoter for the CO sensing properties. Therefore, studies were extended to several Au concentrations on TiO_2 and, in addition, to simultaneous loads of Au and Nb or V. Doubly modified Au-and Nb-TiO_2 presented the highest Au content on surface, as confirmed by XPS measurements, and exhibited the largest and fastest sensor response to CO at high operating temperatures.

Castañeda [117] reported that titanium dioxide (TiO_2-anatase phase) thin films were deposited by the ultrasonic spray pyrolysis technique employing titanium (IV) oxide acetylacetonate ($TiO(acac)_2$) dissolved in pure methanol as a source material. In order to prepare oxygen sensors, TiO_2 thin films were deposited on interdigitated gold electrodes

with contacted alumina substrates. Palladium (Pd) coatings were carried out by vacuum thermal evaporation through a metallic mask. The effect of the surface additive (Pd) on the response of the thin film TiO_2 oxygen sensors was monitored in a mixture with zero-grade air. The electrical characterization (monitoring of the electrical surface resistance with the operation temperature) of the sensors in an atmosphere of oxygen (diluted in zero-grade air) was performed in a vacuum chamber (10^{-6} Torr), where the gas pressure can be controlled. The films sensitivity was estimated by the following relation: $S = (R_{gas}-R_0)/R_0$. The response time of the sensor is defined to be the time needed to reach a $0.9R_0$ value when the oxygen excess was removed. The gas-sensing properties of TiO_2 sensors in an atmosphere of 10^4 ppm of oxygen were measured between 100 and 450 ^oC. Experimental results obtained using palladium as a surface additive showed that the sensitivity reached a stationary value of 1.18 for O_2 concentration of 100 ppm in zero-grade air at 300 ^oC, which was as high as those reported for oxygen sensors prepared with more expensive and complex techniques. The role and activity of palladium coatings incorporated on solid-state oxygen sensors were determined by their chemical state, aggregation form and interaction with the metal-oxide semiconductor.

Manera *et al.* [118] investigated the optical gas sensing properties of pure TiO_2 thin films and with inclusion of dot- and rod-shaped gold nanoparticles (NPs) prepared by a sol-gel method and annealed at 200^oC. The obtained nanostructures were analyzed from both optical and morphological points of view. In particular, the prepared films showed interesting dynamic optical absorption sensing responses towards different kinds of alcohol vapors in the spectral range corresponding to the surface plasmon resonance (SPR) peak of the gold nanoparticles. Total attenuation surface plasmon resonance measurements in controlled atmosphere demonstrated a

sensing activity due to variation of the thickness.

Phanichphant *et al*. [119] reported that unloaded TiO_2 and TiO_2 nanoparticles loaded with 1–5 at.% Nb were successfully produced in a single step by FSP. The sensing films were prepared by spin coating technique. The mixing sample was spin-coated onto the Al_2O_3 substrates interdigitated with Au electrodes. The gas sensing of acetone (25–400 ppm) was studied at operating temperatures ranging from 300–400 ^oC in dry air, while the gas sensing of ethanol (50–1,000 ppm) was studied at operating temperatures ranging from 250–400 ^oC in dry air. The 3 at.% Nb-dispersed on TiO_2 sensing film showed a response of 31.7 and a very fast response time of 1 second towards 400 ppm ethanol, as compared to an undoped TiO_2 sensing film. The 3 at.% Nb-dispersed on TiO_2 sensing film also showed a response of 13 and a response time of 33 seconds towards 400 ppm acetone.

Cheng *et al.* [120] reported that monodispersed TiO_2 spherical colloids with diameters of about 250 nm were prepared by a sol-gel method. Heterostructural Ag/TiO_2 spheres were manipulated by surface engineering, in which the Ag nanoparticles with an average size of 10 nm were uniformly distributed on the surface of the TiO_2 nanospheres by *in situ* reduction and growth. The gas-sensing properties of the TiO_2 nanospheres and heterostructural Ag/TiO_2 nanospheres to ethanol and acetone were measured at 350 ^oC. The results indicated that Ag nanoparticles greatly enhanced the response, stability and response characteristic of TiO_2 nanospheres to the tested gases. Response times of Ag/TiO_2 sensor to 30 ppm acetone and 50 ppm ethanol were <5 s.

Zhang *et al.* [121] reported that Pt/TiO_2 sensor exposed to H_2/O_2. The surface of the sensing layer was modified by an H_2PtCl_6-containing solution and treated under different conditions. The sensor treated at 900^oC showed a response time of about 40

millisecond (ms) when exposed to H_2 and 20 ms exposed to O_2 at 500–800 ^oC. Results indicated that the response time, which reflects the rate of change of the sensor resistance, was controlled by the activation energy (*E*). Sensors with lower activation energy exhibited a faster rate of response when the magnitude of response was approximately uniform. The response properties, on the other hand, were promoted by increasing the amount of platinum particles dispersed on the sensor surface via a spill-over effect.

Samerjai *et al.* [122] reported that FSP presented a technique for metal (Pt, Sn, Ru, Nb and W) -loaded metal oxide (MOX) nanoparticle synthesis, which requires only a single step. FSP prepared MOX nanoparticles have recently widely employed for gas-sensing applications. In this work, the performance towards flammable gases of unloaded and metal (Pt, Sn, Ru, Nb and W)-catalyzed metal oxide (ZnO, WO_3, SnO_2 and TiO_2) nanoparticle thick films fabricated by FSP and spin-coating was reviewed, discussed and compared to MOXs prepared by other methods. The gas-sensing characteristics towards H_2, CH_4, C_2H_2, C_2H_4, C_2H_5OH and CO gases of FSP-prepared MOXs were found to be significantly improved in terms of response, response time and selectivity with small Pt, Sn, Ru, Nb and W loading contents ranging from 0.2 to 5 mol% or at.%. In addition, Pt loading on WO_3 and ZnO sensors results in excellent detection performances towards several flammable gases including H_2, CH_4 and C_2H_2.

Srivastava *et al.* [123] reported that ammonia gas sensing properties of a single layer WO_3 thick film and a double layer sensor structure having a supported catalyst on it were investigated. The single layer sensor exhibited low response to NH_3. An enhancement in gas response was achieved by doping WO_3 with Pt, Pd or Au. Ammonia sensing properties of the WO_3 thick film was improved markedly by overcoating a

platinum catalyzed silica-niobia layer onto the WO_3 film surface. Such a double layer structure not only increased the gas response, but decreased the response time also.

Table 1.5 shows the summary on the gas sensing properties of differently prepared unloaded TiO_2 and metal-loaded TiO_2 towards reducing gas.

Table 1.5 A summary on the gas sensing properties of differently prepared unloaded TiO_2 and metal-loaded TiO_2 towards reducing gas

Sensing materials	**Method**	**Gas Concentration**	**Response**	**Reference**
0.5% Pt and 1.0% Nb/TiO_2	Sol-gel method, Spin-coating (sensors)	Methanol ; 500 ppm Ethanol ; 500 ppm	~2.0 at 300 ^oC ~6.5 at 400 ^oC ~5.0 at 500 ^oC ~70 at 300 ^oC ~60 at 400 ^oC ~20 at 500 ^oC	[124]
TiO_2 nanotubes	Screen-printing method (sensors)	Ethanol ; 50 ppm	~ 45 at 450 ^oC	[125]
0.25 wt% Au-loaded TiO_2 nanotubes			~ 72 at 450 ^oC	
0.42 wt% Au-loaded TiO_2 nanotubes			~ 82 at 450 ^oC	
0.92 wt% Au-loaded TiO_2 nanotubes			~ 84 at 450 ^oC	

Table 1.5 (Cont.) A summary on the gas sensing properties of differently prepared unloaded TiO_2 and metal-loaded TiO_2 towards reducing gas

Sensing materials	Method	Gas Concentration	Response	Reference
TiO_2 nanotubes (Obtained by hydrothermal treatments for 24 h, at 230°C)	Screen-printing method (sensors)	H_2 ; 500 ppm CO ; 500 ppm Ethanol ; 47 ppm	~ 10 at 500 °C ~ 8 at 500 °C ~ 15 at 500 °C	[126]
TiO_2 (P25)		H_2 ; 500 ppm CO ; 500 ppm Ethanol ; 47 ppm	~ 9 at 500 °C ~ 13 at 500 °C ~ 25 at 500 °C	
8 wt% Au-TiO_2 nanocomposites (annealed at 500°C)	Sol-gel films	H_2 ; 300 ppm CO ; 300 ppm	~ 53 at 500 °C ~ 1.8 at 500 °C	[127]
Ag-TiO_2 (core/shell)	Spin-coating method (sensors)	Ethanol ; 100 ppm CO ; 100 ppm CH_4; 100 ppm	~ 1.3 at 30 °C ~ 0.3 at 30 °C ~ 0.2 at 30 °C	[128]
TiO_2	Sol-gel method, Dip-coating technique	Ethanol; 100 ppm Methanol; 100 ppm	~ 20 at 400°C ~ 35 at 500°C ~ 7.0 at 400 °C ~ 13 at 500 °C	[31]

Table 1.5 (Cont.) A summary on the gas sensing properties of differently prepared unloaded TiO_2 and metal-loaded TiO_2 towards reducing gas

Sensing materials	Method	Gas Concentration	Response	Reference
TiO_2 nanofibers	Calcination of electrospun TiO_2/PVP composites	CO: 1–15 ppm	~ 2.6 towards 15 ppm at 200 °C	[129]
TiO_2 Ag-TiO_2 spheres	Coated by three-layer paste, sintered at 350°C for 3 h in air to form a thick sensing film.	Ethanol ; 10000 ppm Acetone ; 10000 ppm Ethanol ; 10000 ppm Acetone ; 10000 ppm	~ 15.1 at 350 °C ~ 11.1 at 350 °C ~ 41.7 at 350 °C ~ 47.7 at 350 °C	[130]
Au-TiO_2	Sputtering	CO ; 125 ppm CO ; 60 ppm	~ 4.1 at 230 °C ~ 3.6 at 230 °C	[131]
TiO_2	Sputtering	CO ; 250 ppm	~ 11.5 at 250 °C	[132]
Pure TiO_2 Nb (10 at%) doped TiO_2	Screen-printing method (sensors)	CO; 100 ppm CO; 100 ppm NO_2; 10 ppm	~ 2.7 at 450 °C ~ 1.6 at 450 °C ~ 1.9 at 450 °C	[35]

Table 1.5 (Cont.) A summary on the gas sensing properties of differently prepared unloaded TiO_2 and metal-loaded TiO_2 towards reducing gas

Sensing materials	Method	Gas Concentration	Response	Reference
TiO_2/PtOPt dual-layer sensor	TiO_2 solution was dropped to spun onto the PtO-Pt film	H_2; 4% in air CO; 20% in air NH_3; 20% in air	~ 75 at 180 ºC ~ 20 at 240 ºC ~ 18 at 260 ºC	[33]
TiO_2 nanotubes	Anodization	H_2; 1000 ppm in N_2	~ 500 at 375 ºC ~ 300 at 345 ºC ~ 60 at 290 ºC ~ 30 at 265ºC	[37]

1.10 Objectives of the study

This research focuses on the synthesis of flame-made unloaded and Pt, Au and Ag-loaded TiO_2 nanoparticles and their characterization for use as gas sensors. The main purposes of this study are:

1.10.1 To study the processing of unloaded and metal-loaded (metal = Pt, Au and Ag) TiO_2 nanoparticles by FSP

1.10.2 To characterize the flame-made particles of unloaded and metal-loaded TiO_2 nanoparticles

1.10.3 To study the effect of metals concentrations

1.10.4 To study the application of the nanoparticles as gas sensors

1.11 Usefulness of the Research (Theory and/or Applied)

1.11.1 Unloaded and metal-loaded TiO_2 nanoparticles with high purity and homogeneity will be produced by FSP in a single step.

1.11.2 Knowledge of FSP technique, sensor preparation, and their gas sensing application will be obtained.

1.12 Research plan, methodology and scope

1.12.1 To review literature

1.12.2 To synthesize unloaded TiO_2 and Pt, Au and Ag-loaded TiO_2 nanoparticles by FSP

1.12.3 To characterization the particle properties facilitated by X-ray Diffraction (XRD), Scanning Electron Microscopy (SEM), High Resolution Transmission Electron Microscopy (HRTEM), Energy Dispersive X-ray Spectroscopy (EDS) and Brunauer Emmett Teller (BET)

1.12.4 To test the gas sensing properties of unloaded TiO_2 and Pt, Au and Ag-loaded TiO_2 synthesized by FSP

1.12.5 Discussion and conclusions